published in Advances in Solid State Physics, Vol. 43, 95 (2003).

Optical Spectroscopy of Low-Dimensional Quantum Spin Systems

Markus Grüninger[1], Marco Windt[1], Eva Benckiser[1], Tamara S. Nunner[2], Kai P. Schmidt[3], Götz S. Uhrig[3], and Thilo Kopp[2]

[1] II. Physikalisches Institut, Universität zu Köln, Zülpicher Str. 77, 50937 Cologne, Germany
[2] Experimentalphysik VI, Universität Augsburg, Universitätsstraße 1, 86135 Augsburg, Germany
[3] Institut für Theoretische Physik, Universität zu Köln, Zülpicher Str. 77, 50937 Cologne, Germany

Abstract. Low-dimensional quantum spin systems display fascinating excitation spectra. In recent years, optical spectroscopy was shown to be a powerful tool for the study of these spectra by means of phonon-assisted infrared absorption. We discuss the results of antiferromagnetic S=1/2 cuprates with various topologies: the spinon continuum observed in the weakly coupled chains of $CaCu_2O_3$, two-triplet bound states and the continuum of the two-leg ladders in $(La,Ca)_{14}Cu_{24}O_{41}$, and the bimagnon-plus-phonon spectrum of the bilayer $YBa_2Cu_3O_6$, an undoped parent compound of the 2D high-T_c cuprates. Various theoretical approaches (dynamical DMRG, continuous unitary transformations (CUT), and spin-wave theory) are used for a quantitative analysis. Particular attention is paid to the role of the cyclic four-spin exchange.

The dawn of phonon-assisted infrared absorption of magnetic excitations dates back to 1959, when Newman and Chrenko [1] observed an infrared absorption band at 0.24 eV in the classic three-dimensional (3D) S=1 antiferromagnet NiO. A connection with the antiferromagnetic order was suggested on the basis of the observed temperature dependence. In 1964 Mizuno and Koide [2] proposed that this absorption band reflects the simultaneous excitation of two magnons and one phonon. At that time, the spin dynamics were analyzed only qualitatively on a mean-field level. In 1966, phonon-assisted two-magnon absorption was also reported in cubic $KNiF_3$ [3], which still is considered to be the best realization of the 3D S=1 Heisenberg model [4]. Only in 1995 Lorenzana and Sawatzky [5] rediscovered this idea and proposed that the mid-infrared absorption features observed in the undoped parent compounds of the high-T_c cuprates [6] – the best realization of the 2D S=1/2 square-lattice Heisenberg model – had to be explained in terms of bimagnon-plus-phonon absorption. On the basis of spin-wave theory they performed the first quantitative analysis and obtained an excellent description of the dominant peak [5]. The spectral weight at higher energies (see below, Fig. 13) was tentatively ascribed to higher-order multi-magnon contributions. Due to the reduced dimensionality and the small spin value S=1/2, quantum

effects should be pronounced. Therefore the nature of the spin excitations in the 2D cuprates is still controversial, in particular at high energies [7–12]. The detailed information on the spectral density offered by the infrared data should allow to clarify this point, but it still poses a challenge to theory. The problems in the description of the line shape of the 2D cuprates appear particularly conspicuous in comparison with the excellent description obtained (a) in spin-wave theory for the isostructural S=1 compound La_2NiO_4 [5,13] and (b) in a two-spinon analysis of the S=1/2 chain Sr_2CuO_3 [14,15]. In 1D good agreement is obtained because quantum fluctuations are fully included, and in the 2D S=1 nickelate because fluctuations beyond spin-wave theory are small. Here, we try to shed some light on this issue by comparing S=1/2 cuprate compounds with different topologies: weakly coupled chains, two-leg ladders and 2D layers. Before, we will discuss bimagnon-plus-phonon absorption in general, the experimental determination of the magnetic contribution to the optical conductivity $\sigma(\omega)$ and in particular the magnetic excitations of S=1/2 two-leg spin ladders.

1 Bimagnon-Plus-Phonon Absorption

This technique allows to study the spin–spin correlation function via a measurement of the dipole–dipole correlation function, i.e., the optical conductivity $\sigma(\omega)$. Since spin is conserved, $\sigma(\omega)$ reflects S=0 excitations (neglecting spin–orbit coupling), e.g., the excitation of two S=1 magnons with total spin $S_{\rm tot}$=0 or the appropriate combination of two elementary triplets (henceforth called *triplons* [16]) or two spinons. However, in the cuprates direct absorption of, e.g., two magnons is not infrared active due to inversion symmetry. We can effectively avoid this selection rule by simultaneously exciting a Cu-O bond-stretching phonon that breaks the symmetry. Hence, the lowest order infrared-active magnetic absorption is a two-magnon-plus-phonon process. The phonon participation was verified experimentally by the observation of a frequency shift induced by oxygen isotope substitution in $YBa_2Cu_3O_6$ [7].

The quantitative analysis [5] starts from a three-band Peierls–Hubbard model in the presence of an electric field $\boldsymbol{E}$. The dominant contribution to the dipole moment arises from displacements of the oxygen ions (only Einstein phonons are considered). These modulate the hopping matrix elements and the on-site energies, whereas the electric field contributes only to the on-site energies. In perturbation theory a low-energy Hamiltonian is derived, in which the relevant term corresponds to a nearest-neighbor Heisenberg Hamiltonian, where the exchange coupling $J_{i,\delta}$ depends on the electric field $\boldsymbol{E}$ and on the displacements of the oxygen ions $\boldsymbol{u}_j$

$$H = \sum_{i,\delta} J_{i,\delta}(\boldsymbol{E}, \{\boldsymbol{u}_j\}) \boldsymbol{S}_i \boldsymbol{S}_{i+\delta} \; . \tag{1}$$

Here, i labels the Cu sites and δ runs over nearest-neighbor sites. We expand $J(\boldsymbol{E}, \boldsymbol{u})$ to order $\partial^2 J / \partial \boldsymbol{E} \partial \boldsymbol{u}$ which entails the coupling of a photon

to a phonon and two neighboring spins. The dipole moment associated with two-magnon-plus-phonon absorption then results from the Fourier transform of the product of neighboring spin operators weighted by a momentum-dependent vertex function $\gamma(k)$, which corresponds to the Fourier transform of $\partial^2 J/\partial \boldsymbol{E}\partial \boldsymbol{u}$. To zeroth order in the magnon–phonon coupling, the magnetic system and the phonon system can be decoupled. The role of the phonon is thus reduced to (a) breaking the symmetry, (b) a shift of the energy scale by the phonon energy ω_{ph}, and (c) a contribution k_{ph} to the total momentum k_{tot}. Since k_{ph} runs over the entire Brillouin zone, the selection rule $0 = k_{\mathrm{tot}} = k_{\mathrm{mag}} + k_{\mathrm{ph}}$ tells us that the magnetic excitations have to be integrated over all momenta, where the form factor is given by $|\gamma(k)|^2 \equiv f_{\mathrm{ph}}(k)$.

2 Experimental Determination of the Magnetic Contribution to $\sigma(\omega)$

Since the considered bimagnon-plus-phonon absorption is a higher-order process, one expects only a weak dipole moment or a small spectral weight in $\sigma(\omega)$. This can be determined very accurately by measuring both the transmittance $T(\omega)$ and the reflectivity $R(\omega)$. The optical conductivity $\sigma(\omega) = n\kappa\omega/2\pi$ results from inverting [17,18]

$$R(\omega) = \frac{(n-1)^2 + \kappa^2}{(n+1)^2 + \kappa^2} \,, \quad T(\omega) = \frac{(1-R)^2 \Phi}{1-(R\Phi)^2} \,, \tag{2}$$

$$\Phi(\omega) = \exp(-2\omega\kappa d/c) = \exp(-\alpha d) \,, \tag{3}$$

where n denotes the index of refraction, κ the extinction coefficient, α the absorption coefficient, c the velocity of light and d the thickness of the transmittance sample [$R(\omega)$ denotes the single bounce reflectivity and hence needs to be measured on a thick ("semi-infinite"), opaque sample]. These equations are obtained for a sample with parallel surfaces by adding up the intensities of all multiply reflected beams *incoherently*, i.e., by neglecting interference effects. Experimentally, this condition is realized either if the sample surfaces are not perfectly parallel or by smoothing out the Fabry–Perot interference fringes by means of Fourier filtering. In case of weak absorption $\kappa \ll n$, the reflectivity is entirely determined by n and not suitable to derive κ by using a Kramers–Kronig transformation. At the same time, κ can be determined very accurately from the transmittance. Since $T(\omega)$ depends exponentially on $\kappa \cdot d$, the appropriate choice of d is essential.

As an example we plot in Fig. 1 the data of the two-leg S=1/2 ladder $\mathrm{La}_x\mathrm{Ca}_{14-x}\mathrm{Cu}_{24}\mathrm{O}_{41}$ [19] (see also Sect. 3). The top panel shows the reflectivity measured on a 0.8 mm thick sample (x=4) for two different polarizations of the electrical field, namely, parallel to the rungs and parallel to the legs. The feature at about 600–700 cm^{-1} corresponds to the Cu-O bond-stretching

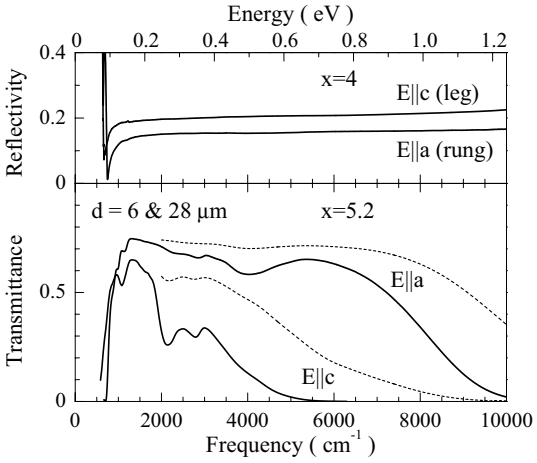

Fig. 1. Mid-infrared reflectivity and transmittance of $La_xCa_{14-x}Cu_{24}O_{41}$ at T=4 K for polarization parallel to the rungs and to the legs, respectively. (**Top panel**) Reflectivity for x=4. (**Bottom panel**) Transmittance of two single crystals with thickness d=28 μm (*solid lines*) and 6 μm (*dashed lines*)

phonon mode. At higher frequencies, the reflectivity is featureless, which is characteristic for an insulator in the regime of weak absorption below the gap. The different absolute values of the two polarization directions reflect the difference in n, namely, $n_a \approx 2.3$ and $n_c \approx 2.6$.

The bottom panel of Fig. 1 shows $T(\omega)$ measured on thin single crystals with x=5.2 for two different thicknesses, d=6 μm and 28 μm. Fabry–Perot interference fringes have been removed by Fourier filtering. In contrast to the reflectivity, the transmittance reveals the weak absorption features we are looking for, in this case in the range from about 2000 to 6000 cm^{-1}. The spectra can be divided into three different regimes. The absorption below $\approx 1300\,\mathrm{cm}^{-1}$ can be attributed to phonons and multi-phonon bands. The strong absorption at high frequencies is due to an electronic background, which has to be identified with the onset of charge-transfer excitations or with the absorption of localized carriers (located in the CuO_2 chains but not in the ladders [20]). In order to analyze the magnetic excitations in the intermediate frequency range, they have to be separated from the background, which thus needs to be known precisely. This requires the measurement of a thin sample, which still is transparent at high frequencies, whereas the weaker magnetic features can be determined more precisely from the data of the thicker sample (see bottom panel of Fig. 1).

The spectrum of the optical conductivity $\sigma(\omega)$ is shown in Fig. 2 for polarization parallel to the legs (top) and parallel to the rungs (middle). In the latter case, the features between 2000 and 6000 cm^{-1} are clearly separated from the high-frequency background, which can be determined unambiguously by a Gaussian fit for $\omega > 7000\,\mathrm{cm}^{-1}$ (dashed line in the middle panel of Fig. 2, see also [17]). For polarization parallel to the legs, the stronger absorption complicates the determination of the background considerably [21]. The data clearly reveal a comparably strong absorption peak at about 6000 cm^{-1},

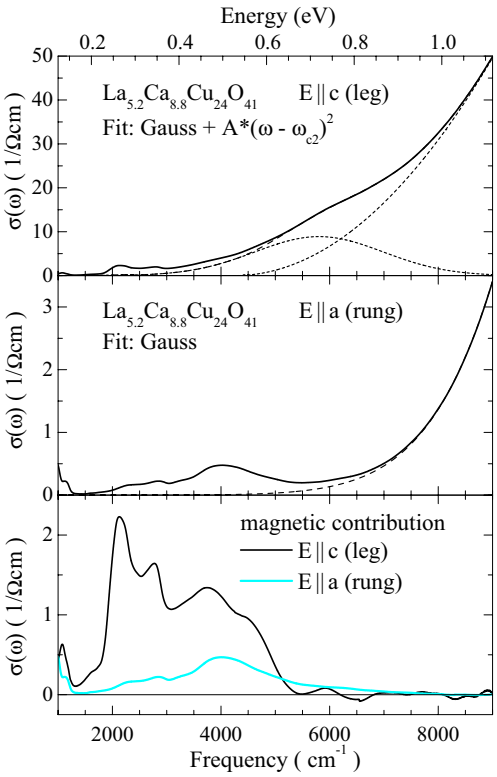

Fig. 2. Optical conductivity $\sigma(\omega)$ of $La_{5.2}Ca_{8.8}Cu_{24}O_{41}$ at T=4 K (*solid lines*) and fits of the high-frequency background (*dashed lines*). (**Top panel**) Polarization parallel to the legs. The total fit (*long-dashed line*) is the sum of a Gaussian and of a quadratic part. (**Middle panel**) Polarization parallel to the rungs. (**Bottom panel**) Magnetic contribution to $\sigma(\omega)$ resulting after subtraction of the background

which can already be seen in $T(\omega)$ of the 6 µm sample (Fig. 1). We obtained an excellent fit by using a Gaussian line shape for this peak plus a quadratic frequency dependence of the absorption at higher frequencies (dashed lines in Fig. 2). Subtracting the background fits we obtain the magnetic contribution to $\sigma(\omega)$ (bottom panel of Fig. 2).

3 Magnetic Excitations of Two-Leg Spin-1/2 Ladders

Two-leg spin-1/2 ladders show fascinating properties such as a spin-liquid ground state with a spin gap to the lowest excited state and superconductivity under pressure upon hole doping [22]. This possibility of hole doping has placed the so-called telephone-number compounds $A_{14}Cu_{24}O_{41}$ in the focus of attention. Here, we are interested in the magnetic properties of nominally undoped samples, i.e. Cu^{2+}, which corresponds to $La_xCa_{14-x}Cu_{24}O_{41}$ with x=6. Single-phase crystals could only be synthesized for $x \leq 5.2$ [23]. However, polarized x-ray absorption data [20] show that at least for $x > 2$ the holes are located within the second structural unit of these compounds, the CuO_2 chains. Thus, we consider the ladders to be undoped [17,19].

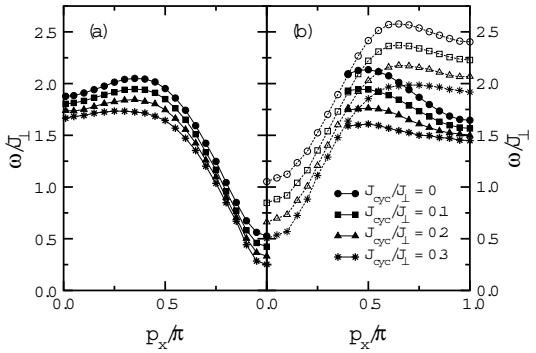

Fig. 3. DMRG results for an 80-site ladder with $J_\parallel = J_\perp$ and $0 \leq J_{\rm cyc}/J_\perp \leq 0.3$ [24]. (**a**) Dispersion of the elementary triplet (triplon) branch. (**b**) Corresponding lower edge of the two-triplon continuum (*open symbols*) and the S=0 two-triplon bound state (*full symbols*)

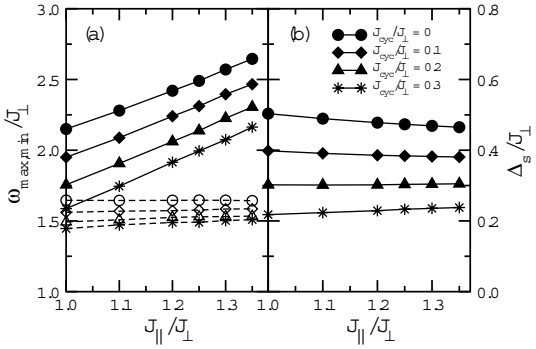

Fig. 4. DMRG results for the bound states and for the spin gap [24]. All results were extrapolated to an infinite ladder. (**a**) Frequency of the maximum of the S=0 bound-state dispersion at $p_x \approx \pi/2$ (*full symbols*) and of the minimum at $p_x = \pi$ (*open symbols*). (**b**) Spin gap Δ_s as a function of $J_\parallel/J_\perp$ for different values of $J_{\rm cyc}/J_\perp$

The minimal model for S=1/2 cuprate ladders consists of an antiferromagnetic Heisenberg Hamiltonian plus an additional cyclic exchange term $H_{\rm cyc}$ [24]

$$\mathcal{H} = J_\parallel \sum_i (\mathbf{S}_{i,l}\mathbf{S}_{i+1,l} + \mathbf{S}_{i,r}\mathbf{S}_{i+1,r}) + J_\perp \sum_i \mathbf{S}_{i,l}\mathbf{S}_{i,r} + H_{\rm cyc} \ , \tag{4}$$

where $J_\perp$ and $J_\parallel$ denote the rung and leg couplings, i refers to the rungs, and l, r label the two legs. The cyclic exchange term[1] corresponds to the cyclic permutation of four spins on a plaquette and emerges as the dominant correction to the nearest-neighbor Heisenberg model in an expansion of the three-band Hubbard model [28]. Rewriting the Hamiltonian in terms of rung singlets and rung triplets, one can easily see that the strongest effect of the cyclic exchange coupling $J_{\rm cyc}$ is a renormalization of the other terms in the Hamiltonian, causing a redshift of the entire one-triplon dispersion (see Fig. 3a) [24]. Correspondingly, also the lower edge of the two-triplon continuum shifts to lower energies (open symbols in Fig. 3b). Below the continuum,

[1] Note that the formulations of $H_{\rm cyc}$ used in the DMRG and in the CUT calculations are slightly different [24,25]. The resulting Hamiltonian is identical except for couplings along the diagonals if $J_\perp$ and $J_\parallel$ are suitably redefined [26].

there exists an S=0 two-triplon bound state (full symbols in Fig. 3b), which results from an attractive interaction between two triplons. The only qualitatively new contribution of the cyclic exchange is a competing *repulsive* interaction between triplets on neighboring rungs. Increasing $J_{\rm cyc}$ thus reduces the binding energy of the two-triplon bound state and also the width of the bound-state dispersion.

The existence of two-triplon bound states in undoped two-leg ladders was predicted theoretically by a number of groups [30–35]. Jurecka and Brenig [33] predicted that the S=0 bound state dominates the optical conductivity spectrum for small values of $J_\parallel/J_\perp$. The evolution of $\sigma(\omega)$ for $0.2 \leq J_\parallel/J_\perp \leq 1.15$ was discussed in [17]. The existence of the S=0 two-triplon bound state was confirmed experimentally by measuring $\sigma(\omega)$ of $(La,Ca)_{14}Cu_{24}O_{41}$ [19]. As shown in Fig. 3b, the bound state shows a maximum at $k \approx \pi/2$ and a minimum at the Brillouin zone boundary. Both give rise to van Hove singularities in the density of states which cause peaks in $\sigma(\omega)$. Knowledge of these two peak frequencies and of the spin gap is sufficient to determine the three coupling constants $J_\parallel$, $J_\perp$ and $J_{\rm cyc}$ (see Fig. 4). For $La_{5.2}Ca_{8.8}Cu_{24}O_{41}$ we find $J_\parallel/J_\perp \approx 1.25$–$1.35$, $J_{\rm cyc}/J_\perp \approx 0.20$–$0.27$, and $J_\perp \approx 950$–$1100\,{\rm cm}^{-1}$ [24]. Inclusion of a sizable $J_{\rm cyc}$ is thus indeed necessary for a consistent description of the experimental data. However, the parameters were determined from three discrete energies. A comparison of the *entire* spectral density calculated for this parameter set with the experimentally determined line shape of $\sigma(\omega)$ provides a thorough test whether this minimal model captures all relevant properties. In fact, the agreement between theory and experiment is excellent (see Fig. 5). The two van Hove singularities of the bound state cause the two peaks at about $2140\,{\rm cm}^{-1}$ and $2780\,{\rm cm}^{-1}$ for leg polarization. For polarization parallel to the rungs, the lower bound state is suppressed due to a selection rule [19], and the upper bound-state peak is about $60\,{\rm cm}^{-1}$ higher, which reflects the different frequencies of the phonons involved in the two polarization directions [36]. The continuum above $\approx 3000\,{\rm cm}^{-1}$ is reproduced almost perfectly, in particular for the rung polarization, which experimentally can be identified unambiguously and with high precision. Due to the complications arising from the background subtraction for polarization parallel to the legs (see Sect. 2), the small deviations within the continuum range in the top panel of Fig. 5 are certainly within the experimental accuracy. In this polarization, $\sigma(\omega)$ contains two contributions, where the two legs are excited in-phase ($p_y = 0$) or out-of-phase ($p_y = \pi$). The two-triplon weight and thus also the bound state is contained in the in-phase contribution, whereas the continuum is dominated by the out-of-phase mode, which reflects the excitation of three (or more) triplons.

In [17,19] we have compared $\sigma(\omega)$ of $(La,Ca)_{14}Cu_{24}O_{41}$ with the results of two further theoretical approaches, namely, Jordan–Wigner fermions [37] and continuous unitary transformations (CUT). There, the cyclic exchange was not included. Here, we report for the first time on CUT results for the spectral

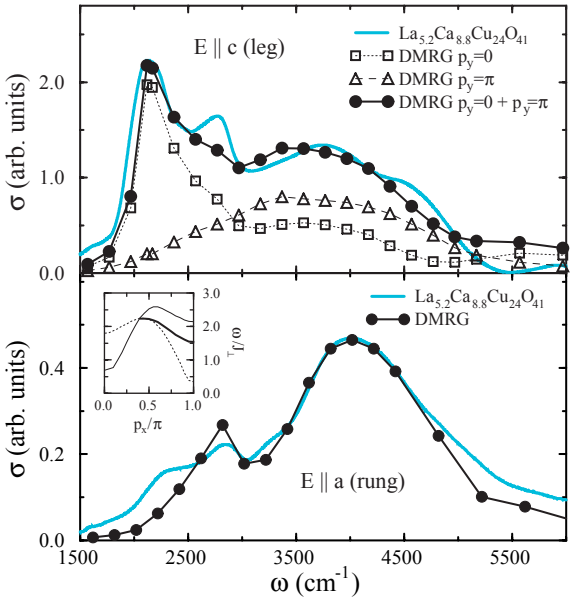

Fig. 5. Comparison of $\sigma(\omega)$ of $La_{5.2}Ca_{8.8}Cu_{24}O_{41}$ at T=4 K (*gray lines*) with DMRG results (*symbols*) [24] for an 80-site ladder with $J_\parallel/J_\perp$=1.3, $J_{cyc}/J_\perp$=0.2, $J_\perp$=1000 cm^{-1}, $\omega_{ph}^{\rm leg}$=570 cm^{-1}, $\omega_{ph}^{\rm rung}$=620 cm^{-1} [29] and a finite broadening of $\delta = 0.1J_\perp$. (**Top panel**) For polarization of the electrical field $\boldsymbol{E}$ parallel to the legs, $\sigma(\omega)$ contains two contributions, in which the two legs are in-phase (p_y=0) or out-of-phase ($p_y = \pi$) with each other. (**Bottom panel**) Polarization parallel to the rungs. (**Inset**) One-triplon dispersion (*dashed line*), lower edge of the two-triplon continuum (*thin solid line*) and S=0 two-triplon bound state (*thick solid line*) for the above parameters

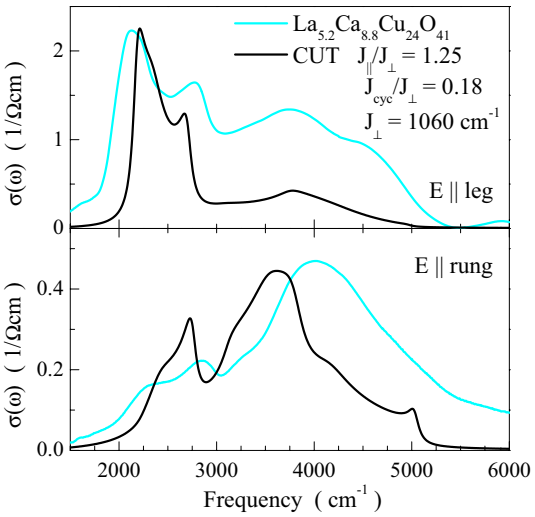

Fig. 6. Comparison of $\sigma(\omega)$ of $La_{5.2}Ca_{8.8}Cu_{24}O_{41}$ (*gray lines*) at T = 4 K with the two-triplon contribution calculated by CUT (*black lines*) for $J_\parallel/J_\perp$ = 1.25, $J_{cyc}/J_\perp$ = 0.18 [26], $J_\perp$ = 1060 cm^{-1}, $\omega_{ph}^{\rm leg}$ = 570 cm^{-1}, $\omega_{ph}^{\rm rung}$ = 620 cm^{-1} [29] and a finite broadening of $\delta = 0.02J_\perp$. (**Top panel**) Polarization parallel to the legs. The missing weight is mainly due to the sizeable three-triplon part (see Fig. 10). (**Bottom panel**) Rung polarization. Here, the leading correction is the small four-triplon part

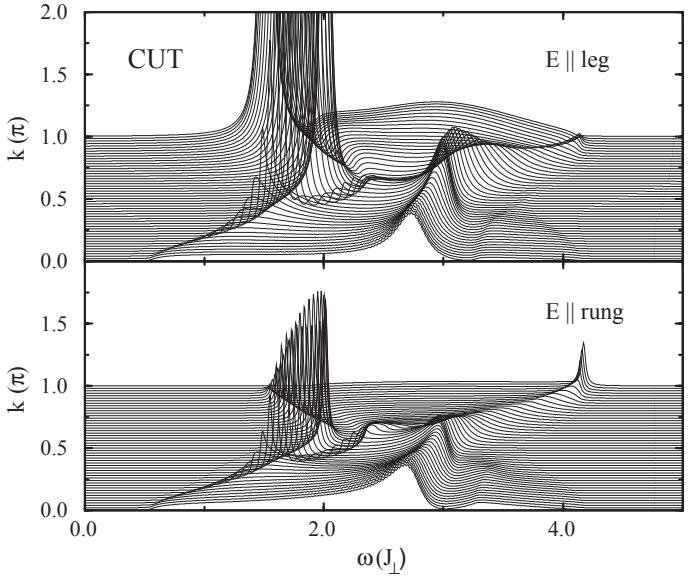

Fig. 7. Momentum-resolved two-triplon spectral densities with $S = 0$ as obtained by the CUT approach for $J_\parallel/J_\perp$=1.25 and $J_{\rm cyc}/J_\perp$=0.18 [26]. (**Top panel**) Polarization parallel to the legs. (**Bottom panel**) Polarization parallel to the rungs

densities including four-spin interactions. In the CUT approach, the Hamiltonian H is mapped to an effective Hamiltonian $H_{\rm eff}$ which conserves the number of rung triplons [38,39]. The ground state of $H_{\rm eff}$ is the rung-triplon vacuum. The CUT is implemented perturbatively in $J_\parallel/J_\perp$ and $J_{\rm cyc}/J_\perp$. The resulting plain series are represented in terms of the variable $1-\Delta_s/(J_\parallel+J_\perp)$ [40,41], where Δ_s is the one-triplon gap which is proportional to the inverse correlation length of the system. Then standard Padé extrapolations yield reliable results up to $J_\parallel/J_\perp \approx$ 1–1.5 depending on the value of $J_{\rm cyc}/J_\perp$.

The CUT result for the two-triplon contribution to $\sigma(\omega)$ is given in Fig. 6 for $J_\parallel/J_\perp$=1.25, $J_{\rm cyc}/J_\perp$=0.18 and $J_\perp$=1060 cm^{-1} [26]. For the comparison with the experimental data one has to bear in mind that the spectral weight of three and more triplons is missing (see Fig. 10 below; note that the rung polarization contains only excitations of an *even* number of triplons). Roughly speaking, the two-triplon contribution calculated by CUT is equivalent to the in-phase contribution of the DMRG result (for leg polarization). Qualitatively, the spectra agree very well with each other. In principle no extra broadening is needed in CUT, thus sharp features are better resolved. However, CUT slightly underestimates the splitting of the two peaks of the bound state and also the position of the continuum in the rung polarization (the frequency of the maximum is too low by about 10%).

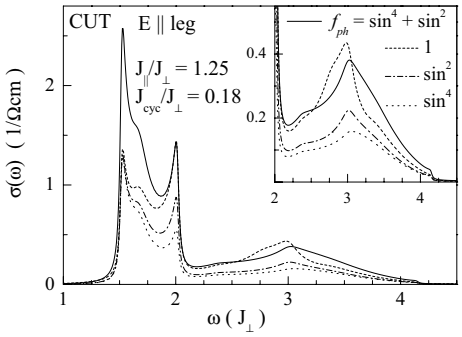

Fig. 8. Influence of the phonon form factor $f_{\rm ph}$ on the line shape of the two-triplon contribution to $\sigma_{\rm leg}(\omega)$ as calculated by CUT for $J_\parallel/J_\perp$=1.25 and $J_{\rm cyc}/J_\perp$=0.18 [26]. (**Inset**) Continuum on an enlarged scale

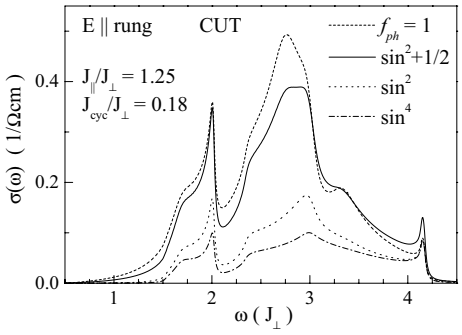

Fig. 9. Influence of the phonon form factor $f_{\rm ph}$ on the line shape of the two-triplon contribution to $\sigma_{\rm rung}(\omega)$ as calculated by CUT for $J_\parallel/J_\perp$=1.25 and $J_{\rm cyc}/J_\perp$=0.18 [26]

The optical conductivity $\sigma(\omega)$ reflects a weighted superposition of the momentum-resolved spectral densities with $S=0$ (see above). The k-resolved CUT data for the two-triplon contribution are shown in Fig. 7. In both panels the spectral densities are dominated by the bound state, which leaves the continuum at $k \approx 0.3\pi$. In both polarizations, the continua show interesting structures. For $0 \le k \le \pi/2$ there is a dominant ridge which develops from the two-triplon Raman peak at k=0. For large k this ridge moves to higher energies, getting an almost anti-bound state at $k=\pi$. In the rung polarization, there is a pronounced feature concentrated around $k = \pi/2$ below the ridge. This feature survives the k integration as a small shoulder in $\sigma(\omega)$, which may correspond to the experimentally observed peak at about $3200\,{\rm cm}^{-1}$ (see bottom panel of Fig. 6). The strength of this feature depends on the weight factor or phonon form factor $f_{\rm ph}$. To lowest order (4th order in the Cu-O hopping t_{pd}), the dominant contribution to $f_{\rm ph}^{\rm leg}$ comes from the in-phase and the out-of-phase stretching modes of the oxygen ions on the legs, whereas for $f_{\rm ph}^{\rm rung}$ the out-of-phase stretching mode and the vibration of the oxygen ion on the rung are taken into account (see also [36])

$$f_{\rm ph}^{\rm leg} = 8\sin^4(\frac{p_x}{2})\,, \quad f_{\rm ph}^{\rm rung} = 8\sin^2(\frac{p_x}{2}) + 4\,. \tag{5}$$

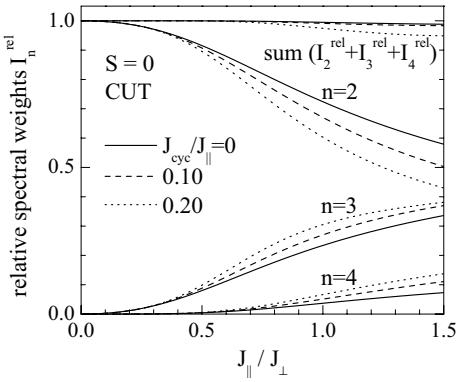

Fig. 10. Relative spectral weights $I_n^{\rm rel}$ of the n-triplon contributions to the S=0 spectral density in leg polarization as a function of $J_\parallel/J_\perp$ for three different values of $J_{\rm cyc}/J_\parallel$ [26]

The effect of different form factors on the line shape of $\sigma(\omega)$ is visualized in Figs. 8 and 9. The small shoulder discussed above at about 2.3 $J_\perp$ is more pronounced for form factors which suppress the dominant ridge at small k. Obviously, both the spectral weight and the line shape depend sensitively on the form factor.

Finally, we discuss the influence of $J_{\rm cyc}$ on the spectral weight and the line shape of $\sigma(\omega)$. The relative spectral weights $I_n^{\rm rel}$ of the n-triplon contributions to the S=0 spectral density calculated by CUT for leg polarization are plotted in Fig. 10 for three different values of $J_{\rm cyc}/J_\parallel$ (see [39] for the S=1 channel). For $J_\parallel$=0 the system consists of local rung singlets which can only be excited to local rung triplets. Due to the local nature, the S=0 weight is exhausted entirely by the two-triplon part, $I_2^{\rm rel}=1$. For finite $J_\parallel$ the two-triplon spectral weight is reduced and the multi-triplon weight is enhanced. In $\sigma(\omega)$ this translates into a spectral weight transfer from low energies to high energies, i.e., to an increase of the high-energy continuum weight. An additional suppression of the leading two-triplon part takes place upon increasing $J_{\rm cyc}$ (see Fig. 10). This reflects the fact that the rung-singlet phase is destabilized by $J_{\rm cyc}$, resulting in a quantum phase transition to the topologically different staggered dimer phase [41–44]. For $J_\parallel/J_\perp = 1.25$ we find a reduction from $I_2^{\rm rel} = 0.64$ for $J_{\rm cyc} = 0$ to $I_2^{\rm rel} = 0.50$ for $J_{\rm cyc}/J_\parallel = 0.2$, i.e., the two-triplon contribution looses about 20% of its weight. The sum of $I_2^{\rm rel}$, $I_3^{\rm rel}$, and $I_4^{\rm rel}$ is very close to 1 at least for $J_\parallel/J_\perp \leq 1.5$ and $J_{\rm cyc}/J_\parallel \leq 0.2$, and $I_4^{\rm rel}$ remains small in this parameter range. It will thus be sufficient to determine the two- and three-triplon contributions in order to obtain a reliable description of the line shape of $\sigma(\omega)$.

The influence of $J_{\rm cyc}$ on the line shape of the two-triplon contribution to $\sigma(\omega)$ is visualized in Figs. 11 and 12 for $J_\parallel/J_\perp$=1.0 and 1.3. The spectra follow the trends apparent in Fig. 3b. With increasing $J_{\rm cyc}$, the dispersion of the bound state and thus also the splitting of the two sharp bound-state peaks in $\sigma(\omega)$ are significantly reduced. Furthermore, an increase of $J_{\rm cyc}$ causes a redshift of the entire spectrum. Additionally, $J_{\rm cyc}$ gives rise to new fine structure

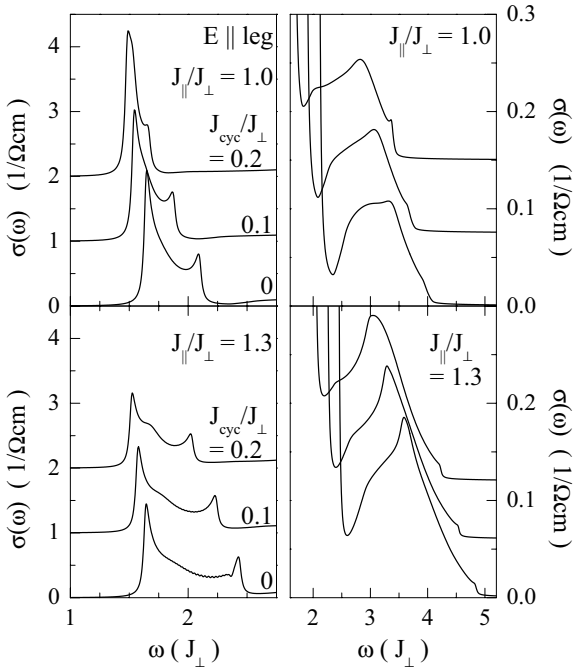

Fig. 11. Influence of $J_{\rm cyc}$ on the line shape of the two-triplon contribution to $\sigma_{\rm leg}(\omega)$ as calculated by CUT [26]. For a direct comparison with the experimental result for $\sigma(\omega)$, one must bear in mind that the sizeable three-triplon contribution is missing (see Fig. 10)

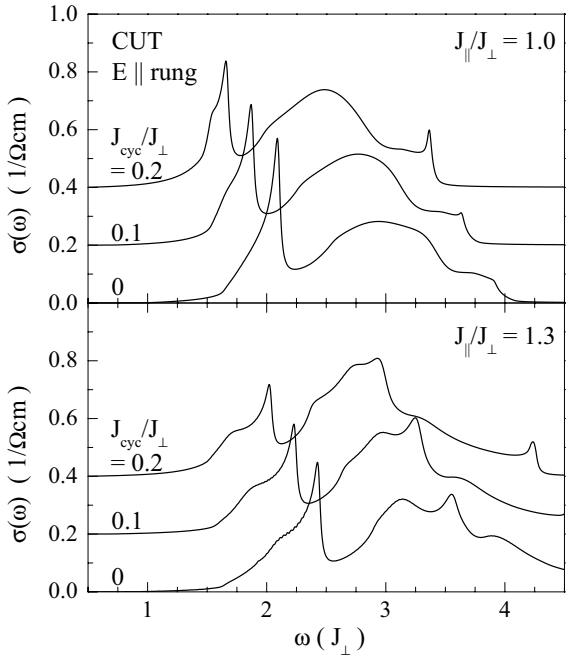

Fig. 12. Influence of $J_{\rm cyc}$ on the line shape of the two-triplon contribution to $\sigma_{\rm rung}(\omega)$ as calculated by CUT [26]. Here, the leading correction is the four-triplon contribution, which is of minor importance

in the spectral densities. For instance for $J_{\parallel}/J_{\perp}$=1.3 and $J_{\rm cyc}/J_{\perp}$=0.2 there appears a shoulder *between* the two bound-state peaks in the leg polarization (see lower left panel of Fig. 11). This can be traced back to a matrix-element effect. The momentum-resolved spectral densities plotted in Fig. 7 reveal that the spectral weight of the two-triplon bound state shows a maximum for a value of k close to but not identical with $k = \pi$. After the integration over k the van Hove singularities dominate the spectra, but the maximum still survives as a clear peak. Pronounced effects of $J_{\rm cyc}$ can also be observed in the continua, where the tendency towards an anti-bound state is enhanced by $J_{\rm cyc}$.

4 From Weakly Coupled Chains to 2D Layers

In Fig. 13, we compare the magnetic contribution to $\sigma(\omega)$ of the undoped S=1/2 two-leg ladder $(La,Ca)_{14}Cu_{24}O_{41}$ [19] discussed in the previous sections with the spectra of the 2D bilayer $YBa_2Cu_3O_6$ [7] (bottom panel) and of $CaCu_2O_3$ (top panel) [45]. The latter compound was thought to represent a two-leg ladder with $J_{\parallel} \gg J_{\perp}$, but it rather has to be viewed as a 3D system of weakly coupled chains [45,46]. In order to facilitate the comparison, the spectra are shifted by the respective phonon frequency $\omega_{\rm ph}$, and the frequency is plotted on the scale of the exchange coupling J (where J reflects the coupling along the chains, along the legs and within the layers, respectively). The values of J were determined by comparison with theoretical results. The apparent trend in Fig. 13 is that the spectral weight is shifted to higher energies on going from 1D chains via ladders to 2D layers. This reflects the increase of the number of nearest-neighbor spins ν from 2 in the chain to 3 in the ladder to 4 in a 2D layer. At the same time, the spectral weight is smeared out over a broader frequency range.

In the 2D cuprates, the high-energy continuum at about $4J$ and above remains puzzling [7,8]. The first question one has to address is which part of the weight reflects magnetic excitations and which part has to be subtracted as a background as in the ladders. On the scale of J used in Fig. 13, the very steep onset of charge-transfer excitations occurs only at about 13 J in $YBa_2Cu_3O_6$ [7], and it is rather unlikely that this causes a significant contribution in the range plotted in Fig. 13. At first one might expect that the unexplained spectral weight above the two-magnon part reflects the multi-magnon contribution. However, the high-energy weight is missing also in exact diagonalization results for the square-lattice Heisenberg model [47]. One may speculate whether this failure is due to the still rather small cluster sizes. Lorenzana et al. claimed that inclusion of a cyclic exchange term offers a remedy to this problem [47]. We have shown above that $J_{\rm cyc}$ enhances the high-energy weight also in the ladders (see Fig. 10), but only by about 20%. Since $J_{\rm cyc}/J$ is very similar in the ladders and in the 2D cuprates [47–49], it seems unlikely that $J_{\rm cyc}$ alone can explain the large discrepancy shown

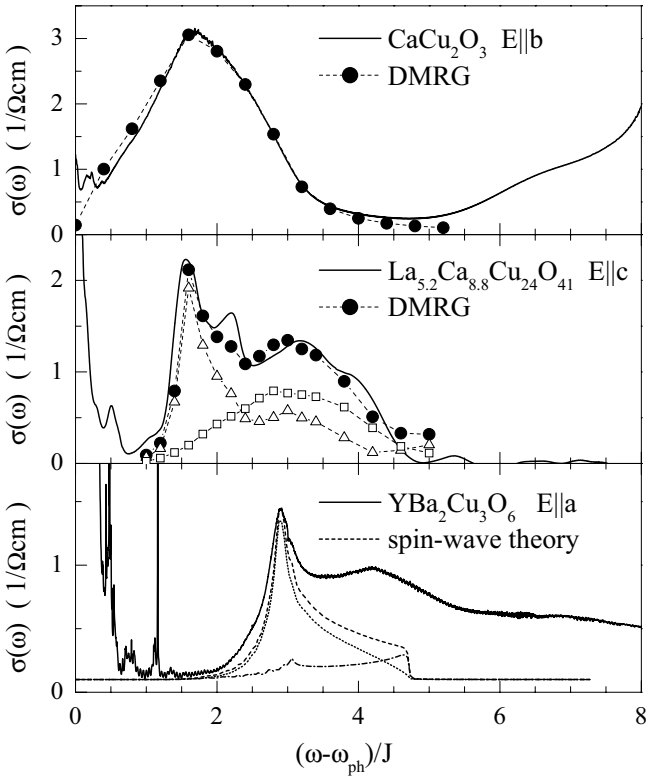

Fig. 13. Evolution of the optical conductivity from weakly coupled chains via two-leg ladders to 2D layers at $T = 4\,\mathrm{K}$. (**Top**) $\sigma(\omega)$ of $CaCu_2O_3$ for $E \parallel b$ (*solid line*), DMRG result (*circles*) for $J_\parallel/J_\perp = 5$ and $J_\parallel = 1300\,\mathrm{cm}^{-1}$ [45]. (**Middle**) $\sigma(\omega)$ of $La_{5.2}Ca_{8.8}Cu_{24}O_{41}$ for $E \parallel c$ (*solid*), DMRG data (*symbols*) for $J_\parallel/J_\perp = 1.3$, $J_{\mathrm{cyc}}/J_\perp = 0.2$ and $J_\parallel = 1000\,\mathrm{cm}^{-1}$ (see Fig. 5) [24]. (**Bottom**) $\sigma(\omega)$ of the 2D bilayer $YBa_2Cu_3O_6$ for $E \parallel a$ (*solid*). In a bilayer, the two-magnon contribution from spin-wave theory (*dashed*) contains an in-plane part (*dotted*) and an inter-plane part (*dash-dotted*). Here, the in-plane exchange is $J = 780\,\mathrm{cm}^{-1}$ and the inter-plane exchange amounts to $J_{12}/J = 0.1$ [7]. The two-magnon peak corresponds to $2.88J$ for $J_{12}/J = 0.1$, and to $2.73J$ for $J_{12} = 0$

in the bottom panel of Fig. 13. Note that in the ladders the discrepancy between the full spectrum and the two-triplon contribution is very similar to the discrepancy observed in the 2D case (see also Fig. 6), which indicates that multi-particle excitations are relevant. Interestingly, all three compounds show a contribution from an *incoherent* continuum at about $2\nu SJ$, where ν denotes the number of nearest-neighbor spins. The position of the continuum thus may reflect the rather local nature of the incoherent excitations. However, in 2D a quantitative description of the total weight still poses a demanding challenge for future research.

Acknowledgements

The single crystals studied here were provided by A. Erb ($YBa_2Cu_3O_6$), C. Sekar and G. Krabbes ($CaCu_2O_3$) and U. Ammerahl, M. Hücker, B. Büchner and A. Revcolevschi (telephone-number compounds). It is a great pleasure to acknowledge their very valuable contribution to this work. We thank D. van der Marel, G.A. Sawatzky, A. Freimuth, C. Knetter and P. Brune for many fruitful discussions. This project is supported by the DFG (SFB 608, SFB 484 and SP 1073) and by the BMBF (13N6918/1).

References

1. R. Newman, R.M. Chrenko: Phys. Rev. **114**, 1507 (1959)
2. Y. Mizuno, S. Koide: Phys. Kond. Mat. **2**, 166 (1964)
3. A. Tsuchida: J. Phys. Soc. Jpn. **21**, 2497 (1966)
4. H. Yamaguchi, K. Katsumata, M. Hagiwara, M. Tokunaga, H.L. Liu, A. Zibold, D.B. Tanner, Y.J. Wang: Phys. Rev. B **59**, 6021 (1999)
5. J. Lorenzana, G.A. Sawatzky: Phys. Rev. Lett. **74**, 1867 (1995); Phys. Rev. B **52**, 9576 (1995)
6. J.D. Perkins, J.M. Graybeal, M.A. Kastner, R.J. Birgeneau, J.P. Falck, M. Greven: Phys. Rev. Lett. **71**, 1621 (1993)
7. M. Grüninger, D. van der Marel, A. Damascelli, A. Erb, Th. Wolf, T. Nunner, T. Kopp: Phys. Rev. B **62**, 12422 (2000)
8. C.-M. Ho, V.N. Muthukumar, M. Ogata, P.W. Anderson: Phys. Rev. Lett. **86**, 1626 (2001)
9. P.W. Anderson: Science **288**, 480 (2000)
10. R.B. Laughlin: Phys. Rev. Lett. **79**, 1726 (1997)
11. G. Aeppli, S.M. Hayden, P. Dai, H.A. Mook, R.D. Hunt, T.G. Perring, F. Dogan: phys. stat. sol. b **215**, 519 (1999)
12. A.W. Sandvik, R.R.P. Singh: Phys. Rev. Lett. **86**, 528 (2001)
13. J.D. Perkins, D.S. Kleinberg, M.A. Kastner, R.J. Birgeneau, Y. Endoh, K. Yamada, S. Hosoya: Phys. Rev. B **52**, R9863 (1995)
14. H. Suzuura, H. Yasuhara, A. Furusaki, N. Nagaosa, Y. Tokura: Phys. Rev. Lett. **76**, 2579 (1996)
15. J. Lorenzana, R. Eder: Phys. Rev. B **55**, R3358 (1997)
16. K.P. Schmidt, G.S. Uhrig: cond-mat/0211627
17. M. Grüninger, M. Windt, T. Nunner, C. Knetter, K.P. Schmidt, G.S. Uhrig, T. Kopp, A. Freimuth, U. Ammerahl, B. Büchner, A. Revcolevschi: J. Phys. Chem. Sol. **63**, 2167 (2002)
18. H.S. Choi, E.J. Choi, Y.J. Kim: Physica C **304**, 66 (1998)
19. M. Windt, M. Grüninger, T. Nunner, C. Knetter, K.P. Schmidt, G.S. Uhrig, T. Kopp, A. Freimuth, U. Ammerahl, B. Büchner, A. Revcolevschi: Phys. Rev. Lett. **87**, 127002 (2001)
20. N. Nücker et al.: Phys. Rev. B **62**, 14384 (2000)
21. In [19] we subtracted an *exponential* background because $T(\omega)$ was restricted to a narrower frequency range. This is not sufficient to fit the more recent high-frequency data of Fig. 2 [17]. For $E \parallel a$, this has only a marginal effect on our estimate of the magnetic contribution to $\sigma(\omega)$. The only relevant difference is an improved description of the high-energy continuum for $E \parallel c$.

22. M. Uehara, T. Nagata, J. Akimitsu, H. Takahashi1, N. Môri, K. Kinoshita: J. Phys. Soc. Jpn. **65**, 2764 (1996)
23. U. Ammerahl, A. Revcolevschi: J. Crystal Growth **197**, 825 (1999); U. Ammerahl: PhD thesis, Univ. of Cologne, 2000
24. T.S. Nunner, P. Brune, T. Kopp, M. Windt, M. Grüninger: Phys. Rev. B **66**, 180404(R) (2002)
25. K.P. Schmidt, C. Knetter, M. Grüninger, G.S. Uhrig: Phys. Rev. Lett. **90**, 167201 (2003)
26. Neglecting two-spin exchange terms along the diagonals, the CUT notation $J_\perp^{\rm CUT}$, $J_\parallel^{\rm CUT}$, $J_{\rm cyc}^{\rm CUT}$ is given in terms of the other notation $J_\perp, J_\parallel, J_{\rm cyc}$ using cyclic permutations by [27] $J_\parallel^{\rm CUT}{=}J_\parallel{+}\frac{1}{4}J_{\rm cyc}$, $J_\perp^{\rm CUT}{=}J_\perp{+}\frac{1}{2}J_{\rm cyc}$, and $J_{\rm cyc}^{\rm CUT}{=}J_{\rm cyc}$.
27. S. Brehmer, H.-J. Mikeska, M. Müller, N. Nagaosa, S. Uchida: Phys. Rev. B **60**, 329 (1999)
28. E. Müller–Hartmann, A. Reischl: Eur. Phys. J. B **28**, 173 (2002), and references therein.
29. Experimentally, the frequency of the upper bound state ω_2 is $\approx 60\,{\rm cm}^{-1}$ higher in $\sigma_{\rm rung}(\omega)$ than in $\sigma_{\rm leg}(\omega)$, thus two different phonon frequencies are used.
30. G.S. Uhrig, H.J. Schulz: Phys. Rev. B **54**, R9624 (1996); erratum *ibid.* **58**, 2900 (1998)
31. K. Damle, S. Sachdev: Phys. Rev. B **57**, 8307 (1998)
32. O.P. Sushkov, V.N. Kotov: Phys. Rev. Lett. **81**, 1941 (1998); V.N. Kotov, O.P. Sushkov, R. Eder: Phys. Rev. B **59**, 6266 (1999)
33. C. Jurecka, W. Brenig: Phys. Rev. B **61**, 14307 (2000)
34. S. Trebst, H. Monien, C.J. Hamer, Z. Weihong, R.R.P. Singh: Phys. Rev. Lett. **85**, 4373 (2000)
35. W. Zheng, C.J. Hamer, R.R.P. Singh, S. Trebst, H. Monien: Phys. Rev. B **63**, 144410 (2001)
36. T.S. Nunner, P. Brune, T. Kopp, M. Windt, M. Grüninger: Acta Phys. Pol. B **34**, 1545 (2003)
37. T.S. Nunner, T. Kopp: cond-mat/0210103
38. C. Knetter, G.S. Uhrig: Eur. Phys. J. B **13**, 209 (2000)
39. C. Knetter, K.P. Schmidt, M. Grüninger, G.S. Uhrig: Phys. Rev. Lett. **87**, 167204 (2001)
40. K.P. Schmidt, C. Knetter, G.S. Uhrig: Acta Phys. Pol. B **34**, 1481 (2003) (cond-mat/0208358)
41. K.P. Schmidt, H. Monien, G.S. Uhrig: to be publ. in Phys. Rev. B (cond-mat/0211429)
42. M. Müller, T. Vekua, H.-J. Mikeska: Phys. Rev. B **66**, 134423 (2002)
43. K. Hijii, K. Nomura: Phys. Rev. B **65**, 104413 (2002)
44. A. Läuchli, G. Schmid, M. Troyer: Phys. Rev. B **67**, 100409 (2003)
45. E. Benckiser, M. Grüninger, T. Nunner, T. Kopp, C. Sekar, G. Krabbes: to be published.
46. T.K. Kim, H. Rosner, S.-L. Drechsler, Z. Hu, C. Sekar, G. Krabbes, J. Malek, M. Knupfer, J. Fink, H. Eschrig: Phys. Rev. B **67**, 024516 (2003)
47. J. Lorenzana, J. Eroles, S. Sorella: Phys. Rev. Lett. **83**, 5122 (1999)
48. R. Coldea, S.M. Hayden, G. Aeppli, T.G. Perring, C.D. Frost, T.E. Mason, S.-W. Cheong, Z. Fisk: Phys. Rev. Lett. **86**, 5377 (2001)
49. A.A. Katanin, A.P. Kampf: Phys. Rev. B **66**, 100403 (2002)